JOURNAL OF PROPULSION AND POWER
Vol. 25, No. 6, November–December 2009

Transient Three-Dimensional Side-Load Analysis of a Film-Cooled Nozzle

Ten-See Wang* and Mike Guidos†
NASA Marshall Space Flight Center, Huntsville, Alabama 35812

DOI: 10.2514/1.41025

Transient three-dimensional numerical investigations on the side-load physics of an engine encompassing a film-cooled nozzle extension and a regeneratively cooled thrust chamber were performed. The objectives of this study are to identify the side-load physics and to compute the associated aerodynamic side load. The computational methodology is based on an unstructured-grid pressure-based computational fluid dynamics formulation and a transient inlet history based on an engine system simulation. Computations simulating engine startup at ambient pressures corresponding to sea level and three high altitudes were performed. In addition, computations for both engine startup and shutdown transients for a stub nozzle operating at sea level were also performed. For engine startups with the nozzle extension attached, computational results show that the dominant side-load physics are the turbine-exhaust-gas-assisted asymmetric Mach disk flow and the subsequent jump of the separation line, which generated the peak side load that decreases as the ambient pressure decreases. For the stub nozzle operating at sea level, the peak side load reduces drastically. The computed side-load physics and the associated peak side load for the sea-level cases agree reasonably well with those of available data from the tests of a similar engine.

Nomenclature

C_1, C_2, C_3, C_μ	=	turbulence modeling constants 1.15, 1.9, 0.25, and 0.09.
C_p	=	heat capacity
D	=	diffusivity
F_{yz}	=	integrated force in the lateral direction
H	=	total enthalpy
K	=	thermal conductivity
k	=	turbulent kinetic energy
p	=	pressure
Q	=	heat flux
T	=	temperature
t	=	time, s
u	=	mean velocities
V^2	=	$\sum u^2$
x	=	Cartesian coordinates or nondimensional distance
α	=	species mass fraction
ε	=	turbulent kinetic energy dissipation rate
θ	=	energy dissipation contribution
μ	=	viscosity
μ_t	=	turbulent eddy viscosity, $\rho C_\mu k^2/\varepsilon$
Π	=	turbulent kinetic energy production
ρ	=	density
σ	=	turbulence modeling constants 0.9, 0.9, 0.89, and 1.15 for Eqs. (2) and (4–6).
τ	=	shear stress
ω	=	chemical species production rate

Subscripts

r	=	radiation
s	=	solid
t	=	turbulent flow
w	=	wall
∞	=	ambient

I. Introduction

STRUCTURAL damages caused by the transient nozzle side loads during testing at sea level have been found for almost all rocket engines during their initial development [1–5]. For example, the J-2 engine gimbal block retaining bolts failed in tension, and the space shuttle main engine (SSME) liquid-hydrogen feed line or steer horn fractured from low cycle fatigue during the shutdown transient [2,5]. More recently, the Japanese LE-7A engine cooling tubes broke [4]. As a final example, during its maiden flight, the European Vulcain engine failed by a leak in coolant pipes allowing the nozzle to overheat; although the side loads were not the root cause, they exacerbated the problem [6]. As a result, whether during sea-level testing or in flight, transient nozzle side load has the potential of causing real system-level failures and are therefore considered to be a high-risk item and a design issue during any new engine development.

The J-2X engine, the Ares I upper-stage engine under development, is an evolved variation of two historic predecessors: the powerful J-2 engine that propelled the upper stages of the Apollo-era Saturn IB and Saturn V rockets, and the J-2S, a derivative of the J-2 that was developed and tested but never flown. Because the asymmetric shock evolutions inside the nozzle, or the origins of the transient nozzle side loads, occur naturally during the nozzle fillup or evacuation processes, it can be safely assumed that the J-2X engine will experience side forces, just like its predecessors such as J-2 and J-2S, or engines similar in design such as the LE-7A and Vulcain engines. It should be noted though that the hardware failures caused by side forces are all fixable or avoidable, once the effect of the side load is understood and the structure is strengthened. For example, the steer horn of the SSME was redesigned to reduce the stress level [2,7]. The strategy is therefore to understand the physics and properly predict the peak side load and its impact on the components during the design phase and before the tests, such that the risk of expensive hardware failures may be avoided or reduced.

Currently, three approaches are available to predict the peak side loads for J-2X: the empirical or skewed-plane approach [5], cold-

Presented as Paper 4297 at the 38th AIAA Fluid Dynamics Conference, Seattle, WA, 22–27 June 2008; received 16 September 2008; accepted for publication 7 July 2009.

*Aerospace Engineer, Mail Stop ER42, Fluid Dynamics Branch, Propulsion Structure, Thermal, and Fluids Analysis Division. Senior Member AIAA.

†Aerospace Engineer, Mail Stop ER21, Liquid Engine and Main Propulsion Systems Branch, Propulsion Systems Design and Integration Division.

flow testing [8], and computational fluid dynamics (CFD) and heat transfer analysis approach [9]. With the advances of computer technology and computational methods, three-dimensional (3-D) time-accurate CFD methodologies have emerged as a useful tool that can simulate asymmetric shock evolutions and predict the associated peak side loads. For example, Yonezawa et al. [10] simulated the startup transient for the LE-7A engine, Boccaletto and Lequette [11] simulated the startup transient for the Vulcain 2 engine, and Wang [9] benchmarked the startup transient for the SSME. Other relevant computational efforts can be found in [3,12,13].

Although LE-7A and Vulcain are main stage engines and J-2X is an upper-stage engine, there is a common feature shared by all three engines: that is, film cooling is used to cool the lower part of the thruster. The difference is that turbine exhaust gas (TEG) is reinjected in J-2X and Vulcain as a film coolant, and pure hydrogen gas is used to cool LE-7A. Compared with the known side-load physics of shock transition and shock breathing of SSME [9], film injection, however, generates additional side-load physics (the interaction of the Mach disk flow with the film coolant flow) that could be significant, as evidenced by the reported broken cooling tubes or the nozzle wall during the early sea-level testing of the LE-7A engine [4]. Several investigations have since been conducted on those additional side-load physics. For example, Boccaletto et al. [14,15] and Reijasse and Boccaletto [16] studied the effect of wall film injection pressure ramping on side loads, and Tomita et al. [17] investigated the effect of step height on side loads.

Because J-2X is an upper-stage engine, in this effort, transient 3-D CFD and heat transfer computations were performed to study the effect of TEG injection on transient side-load physics for high-altitude startups with a preliminary version of the J-2X engine. For sea-level testing purposes, both the startup and shutdown cases of a stub nozzle in which the nozzle extension was removed were studied. Because Watanabe et al. [4] reported drastically reduced sea-level nozzle side load without the nozzle extension, an additional computation was performed for a hypothetical startup case with the nozzle extension attached, to investigate the differences in nozzle side-load reduction with and without the nozzle extension. The results of these computations are presented here with emphases on the peak side-load physics caused by the interactions of the TEG film coolant with the Mach disk flow and on the effects of altitude and reduced nozzle surface area on those interactions.

II. Computational Methodology

A. Computational Fluid Dynamics

The CFD methodology is based on a multidimensional, finite volume, viscous, chemically reacting unstructured-grid and pressure-based formulation. Time-varying transport equations of continuity, species continuity, momentum, total enthalpy, turbulent kinetic energy, and turbulent kinetic energy dissipation were solved using a time-marching subiteration scheme and are written as

$$\frac{\partial \rho}{\partial t} + \frac{\partial}{\partial x_j}(\rho u_j) = 0 \tag{1}$$

$$\frac{\partial \rho \alpha_i}{\partial t} + \frac{\partial}{\partial x_j}(\rho u_j \alpha_i) = \frac{\partial}{\partial x_j}\left[\left(\rho D + \frac{\mu_t}{\sigma_\alpha}\right)\frac{\partial \alpha_i}{\partial x_j}\right] + \omega_i \tag{2}$$

$$\frac{\partial \rho u_i}{\partial t} + \frac{\partial}{\partial x_j}(\rho u_j u_i) = -\frac{\partial p}{\partial x_i} + \frac{\partial \tau_{ij}}{\partial x_j} \tag{3}$$

$$\begin{aligned}\frac{\partial \rho H}{\partial t} + \frac{\partial}{\partial x_j}(\rho u_j H) &= \frac{\partial p}{\partial t} + Q_r + \frac{\partial}{\partial x_j}\left(\left(\frac{K}{C_p} + \frac{\mu_t}{\sigma_H}\right)\nabla H\right) \\ &+ \frac{\partial}{\partial x_j}\left(\left((\mu + \mu_t) - \left(\frac{K}{C_p} + \frac{\mu_t}{\sigma_H}\right)\right)\nabla(V^2/2)\right) + \theta\end{aligned} \tag{4}$$

$$\frac{\partial \rho k}{\partial t} + \frac{\partial}{\partial x_j}(\rho u_j k) = \frac{\partial}{\partial x_j}\left[\left(\mu + \frac{\mu_t}{\sigma_k}\right)\frac{\partial k}{\partial x_j}\right] + \rho(\Pi - \varepsilon) \tag{5}$$

$$\begin{aligned}\frac{\partial \rho \varepsilon}{\partial t} + \frac{\partial}{\partial x_j}(\rho u_j \varepsilon) &= \frac{\partial}{\partial x_j}\left[\left(\mu + \frac{\mu_t}{\sigma_\varepsilon}\right)\frac{\partial \varepsilon}{\partial x_j}\right] \\ &+ \rho\frac{\varepsilon}{k}(C_1\Pi - C_2\varepsilon + C_3\Pi^2/\varepsilon)\end{aligned} \tag{6}$$

B. Computational Heat Transfer in Solids

The solid heat conduction equation for the composite nozzle extension was solved with the gas-side heat flux distributions as its boundary condition. The solid heat conduction equation can be written as

$$\frac{\partial \rho C_p T_s}{\partial t} = \frac{\partial}{\partial x_j}\left(K\frac{\partial T_s}{\partial x_j}\right) \tag{7}$$

A predictor and corrector solution algorithm was employed to provide coupling of the governing equations. A second-order central-difference scheme was employed to discretize the diffusion fluxes and source terms. For the convective terms, a second-order, total-variation-diminishing, upwind-difference scheme was used. To enhance the temporal accuracy, a second-order backward-difference scheme was employed to discretize the temporal terms. Point-implicit method was used to solve the chemical species source terms. Subiterations within a time step were used for driving the system of second-order time-accurate equations to convergence. Details of the numerical algorithm can be found in [18–21].

An extended k-ε turbulence model [22] was used to describe the turbulence. A modified wall function approach was employed to provide wall boundary-layer solutions that are less sensitive to the near-wall grid spacing. Consequently, the model has combined the advantages of both the integrated-to-the-wall approach and the conventional law-of-the-wall approach by incorporating a complete velocity profile and a universal temperature profile [23]. A seven-species, nine-reaction detailed mechanism [23] was used to describe the finite rate hydrogen/oxygen afterburning combustion kinetics. The seven species are H_2, O_2, H_2O, O, H, OH, and N_2. The thermodynamic properties of the individual species are functions of temperature. The multiphysics pertinent to this study have been anchored in earlier efforts (e.g., SSME axial force and wall heat transfer [18], SSME startup side load [9], nozzle film-cooling applications [24], and conjugate heat transfer [25]).

C. Simulated Startup and Shutdown Sequences

The startup and shutdown sequences are important drivers to the nozzle side-load physics. They contain not only the inlet pressure and temperature histories, but also the species-mass-fraction histories. The ramp rate of the pressure sequence generally determines the magnitude and duration of the peak side load. The temperature and species-mass-fraction histories determine the extent of the combustion reactions that in turn affect the magnitude and duration of the peak side load. Another reason the temperature and species composition are important is because they largely determine the specific heat distribution that in turn determines the shock shape, which again impacts the side-load physics. Given another example of the importance of the species composition, if excess fuel is dumped at a certain period of time, combustion waves could occur that add to the severity of the side load.

The startup and shutdown sequences are obtained through system modeling that simulates the transient histories of the aforementioned variables in a network of components and subcomponents, including the valve actions, in a rocket engine. Figure 1 shows the inlet pressure and temperature histories and Fig. 2 shows the inlet species-mass-fraction histories for the main combustion chamber (MCC) and the TEG flows during the startup transient. The transient reactant composition obtained from system modeling at the two inlets was preprocessed with the Chemical Equilibrium Calculation program [26], assuming the propellants were ignited to reach equilibrium composition immediately beyond the injector faceplate. It can be seen from Fig. 1 that the MCC pressure and temperature ramps mainly between 1 and 3 s. However, that does not mean that nothing

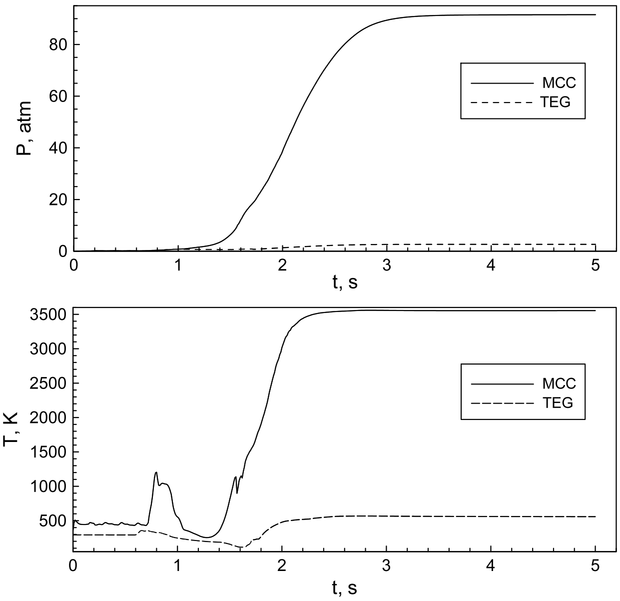

Fig. 1 Simulated inlet pressure and temperature histories for the main combustion chamber and turbine exhaust gas flows during the startup transient.

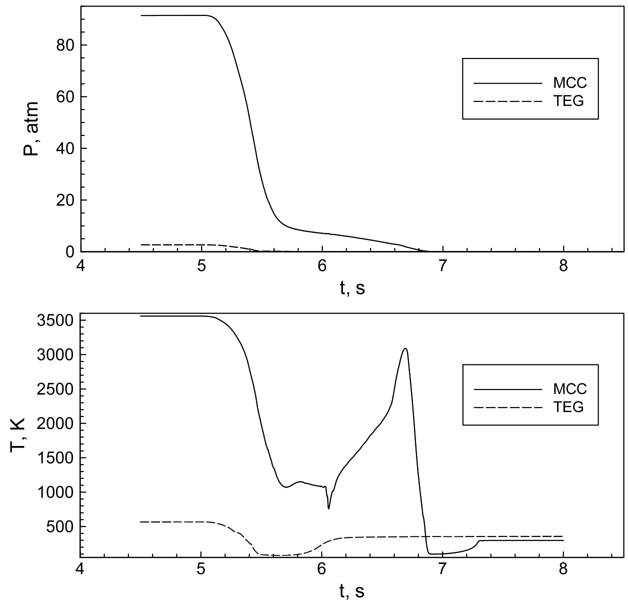

Fig. 3 Simulated inlet pressure and temperature histories for the main combustion chamber and turbine exhaust gas flows during the shutdown transient.

else is happening before 1 s; for example, there is a small temperature spike occurring between 0.75 and 1 s in the MCC, which is caused by combustion of excess hydrogen with oxygen, resulting in a small spike of steam concentration at about the same time frame, as shown in Fig. 2. It can also be seen from Fig. 2 that helium (HE) purge gas enters both the MCC and TEG chamber right after the start command, which has the effect of diluting the fuel concentration in the early startup process and possibly eliminating the occurrence of a potentially hazardous combustion wave [9].

Figure 3 shows the simulated inlet pressure and temperature histories and Fig. 4 shows the inlet species-mass-fraction histories of the MCC and TEG flows during the shutdown process. The species mass fractions appearing in Fig. 4 were again preprocessed assuming chemical equilibrium. It can be seen from Fig. 3 that the pressure and temperature ramp down more rapidly than the startup ramp, with the largest change occurring in the 5.2 to 5.6 s time interval. Again, similar to during the startup process, a temperature spike is shown to occur between 6 and 7 s, caused by the valve sequencing. During that time period, the purge flow downstream of the main oxygen valve (MOV) begins to flow and accelerate the oxygen flow through the injector after the MOV is closed. The main fuel valve (MFV) then also slowly begins to close but does not reach full closure until after the MOV closes. The MCC temperature starts to spike while the remaining oxygen in the main injector is still being purged through the MCC and the fuel to the MCC is being starved due to the closure of the MFV. Helium purge gas again replaces the propellants to close out the shutdown transient. There is a rise of residual fuel concentration in MCC from about 6.8 to 7.2 s, the peak of which is around 6.95 s, which is just behind the peak of the temperature spike in the MCC at around 6.7 s. We will present later that these rises in fuel species concentration and temperature may have caused teepeelike formations on the nozzle wall: an interesting phenomenon but possibly harmless, because the flow rates at this time are fairly small. Note that only traces amount or no oxygen are shown in Figs. 2

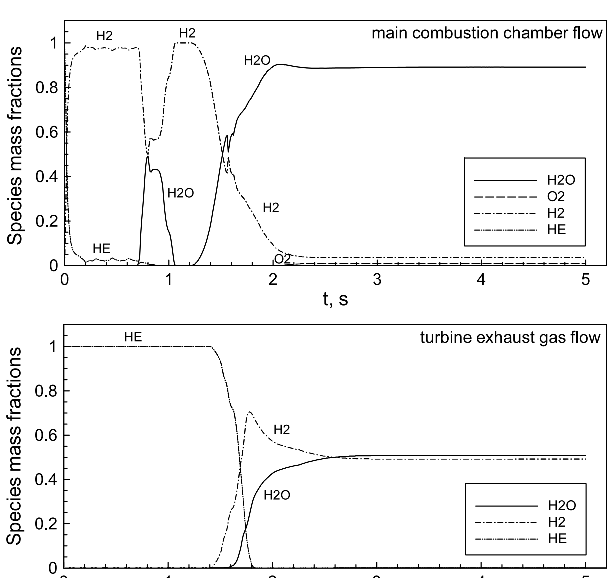

Fig. 2 Simulated inlet species-mass-fraction histories for the main combustion chamber and turbine exhaust gas flows during the startup transient.

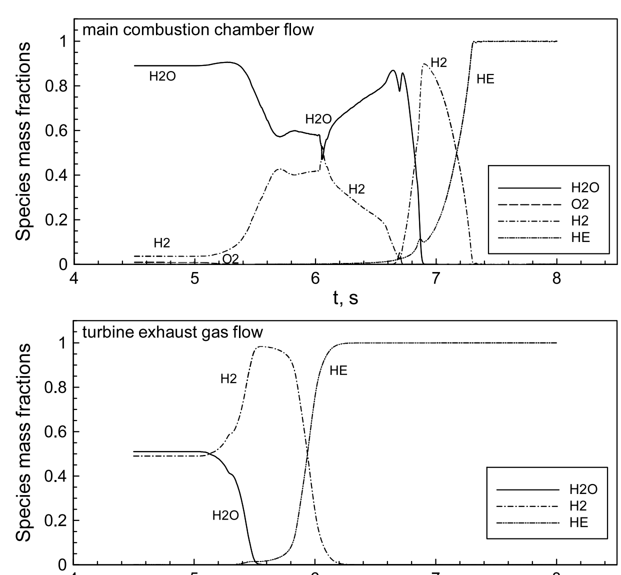

Fig. 4 Simulated inlet pressure and temperature histories for the main combustion chamber and turbine exhaust gas flows during the shutdown transient.

and 4, because the engine is running fuel-rich and most or all of the oxygen is consumed.

III. Computational Grid Generation

The computational domain for the J-2X nozzle side-load investigation includes the MCC, nozzlette for TEG flow injection, nozzle extension, plume, and freestream regions. The general procedure of the grid generation follows that of the SSME benchmark effort [9] by rotating an axisymmetric grid using a software package Gridgen [27]. Figure 5 shows the layout of a typical computational grid. The outer boundaries and the wall boundaries for the MCC, nozzle, nozzlette, and nozzle extension are shown in the top figure. It also shows that the positive x direction is that of the axial flow; hence, the aerodynamic forces exerted in the y and z directions are the side forces. The final 3-D grid is constructed by rotating the axisymmetric grid, shown in the bottom figure of Fig. 5. It can be seen that the cells for the MCC, nozzle, nozzle extension, and plume regions are quadrilateral and those for the freestream region are triangular. After grid rotation, the triangular cells become prisms and the quadrilateral elements become hexagons. The cell shapes are so chosen because the quadrilateral and hexagonal cells are higher-quality cells than those of triangular and prismatic cells [18,28], and higher-quality cells are preferred in the action regions. In addition, the final 3-D grid is symmetric to the central axis, ensuring that the computed asymmetric flow comes from the side-load physics and not an asymmetric grid topology.

Figure 6 shows a close-up look at the grid cells near the nozzlette. The nozzlette generates the TEG flow that cools the nozzle extension. Note that the nozzle extension, a composite material, is a very thin wall and the temperatures on it are solved simultaneously with the fluid dynamics. It should be pointed out that the dimension of the nozzlette is very small in comparison with the nozzle and the nozzle extension. As indicated in Fig. 6, the end of the nozzle is flush with the exit plane of the nozzlette. Also, the inner wall of the nozzlette is tangent and almost coincides with the nozzle wall such that the TEG flow comes out tangent with the nozzle flow, to minimize the impingement between two supersonic jets. In addition, there is no backstep between the core flow and the TEG flow. Any side load potentially caused by that nonexistent backstep is not captured in these simulations.

The geometries of the nozzle and the nozzle extension are truncated ideal contour (TIC) and are only separated by the ring-shaped nozzlette exit plane. The aspect ratios are 35 and 92 for the nozzle and nozzle extension, respectively. A previous study [9] showed that

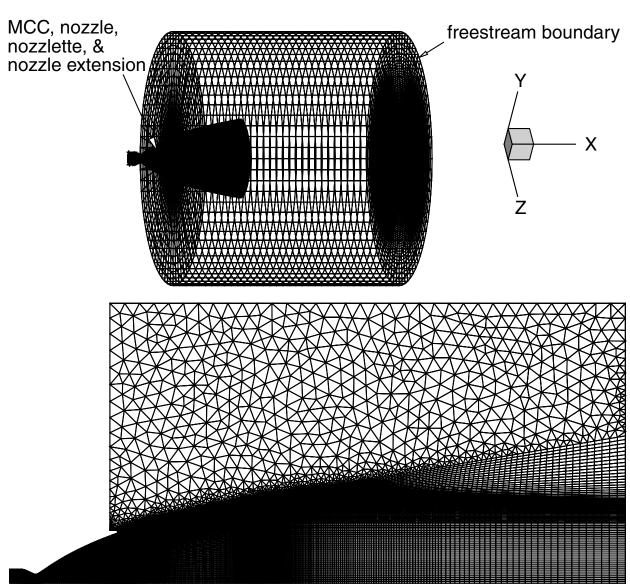

Fig. 5 Layout of a hybrid computational grid: overall view (top) and axisymmetric grid used to construct the final 3-D grid (bottom).

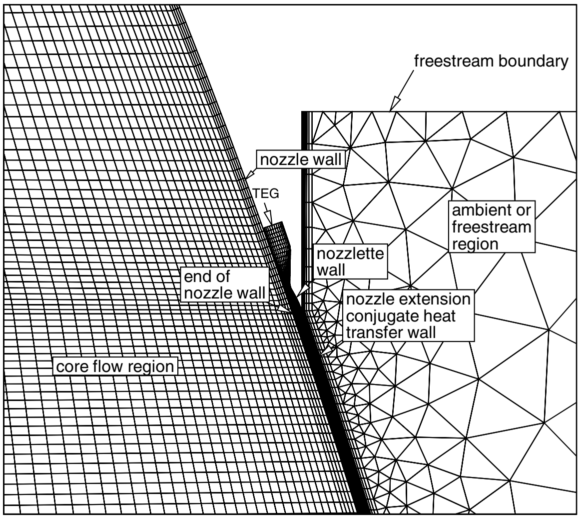

Fig. 6 Close-up view at the hybrid computational grid near the nozzlette that houses the turbine exhaust flow.

performing grid studies on axial force may be an efficient strategy for nozzle side-load applications, assuming that a grid suitable for axial-force calculation is sufficient for side-force calculation. Three 3-D grids containing 1,581,306 (3d1), 2,011,902 (3d2), and 2,148,812 (3d3) grid points were generated and tested for axial-force predictions. Following the layout in [9], the circumferential division number is 72 for all three grids. Grids 3d2 and 3d3 have their grid densities increased in the thruster and plume regions. As a result, grids 3d2 and 3d3 were selected for the transient computations. The total grid points used in these 3-D grids are higher than the 1,286,934 points used for the SSME benchmark [9] and much higher than the 85,000 cells used on Vulcain 2 [11] and the 145,500–405,900 points used for the side-load calculations for the LE-7, LE-7A, and CTP-50-R5-L engines [10].

IV. Boundary and Inlet Conditions

Fixed total conditions were used for the freestream boundaries. Time-varying inlet flow boundary conditions were used at the inlets for the MCC and TEG flows. These time-varying inlet flow properties were obtained from the system simulations that include the time-varying total pressure, temperature, and reactant composition, as shown in Figs. 1–4. The details about the system simulations are discussed earlier. In addition, there was speculation that the radiation from the nozzle extension wall would be significant and should be included in the transient calculations. Four demonstrative steady-state computations were therefore performed with coupled radiation and conjugate heat transfer to see how the radiation would affect the computed axial forces at four different altitudes. The results show that the radiation has negligible impact on all four computed axial forces. As such, it is reasoned that the radiation would have negligible impact on the side force as well. The radiation calculation was hence ignored for the subsequent transient computations. Furthermore, because the combustion chamber and nozzle are regeneratively cooled and it has been shown that the cold wall temperatures due to the regenerative cooling affected whether a free-shock separation (FSS) or a restricted-shock separation (RSS) persisted in the advancing Mach disk flow, which eventually affected the magnitude of the peak side load [9]. A separate conjugate heat transfer calculation was therefore performed with a thermal model and the combustion chamber and nozzle wall temperature profiles were provided as the boundary condition, as shown in Fig. 7. As for the temperatures on the nozzle extension, steady-state conjugate heat transfer computations were performed and the resulting nozzle extension inner wall temperature profile is shown in Fig. 7. For startup transient computations, the thermal wall boundary condition was started out as adiabatic; the wall temperatures shown in Fig. 7

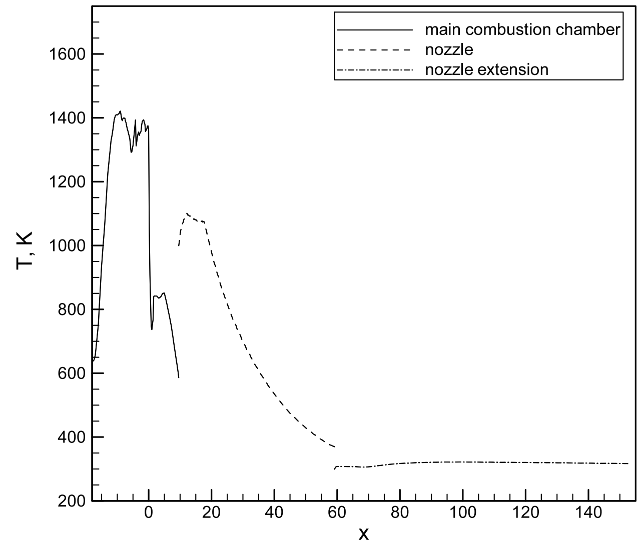

Fig. 7 Temperature boundary condition for the combustion chamber, nozzle, and nozzle extension.

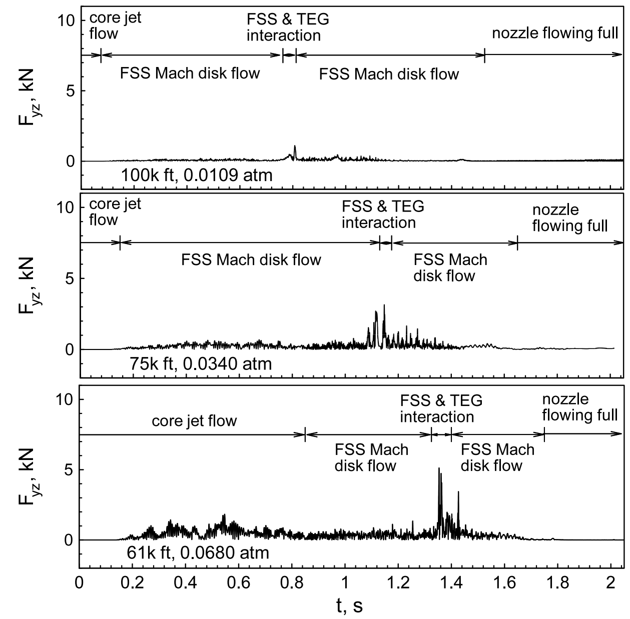

Fig. 8 Computed side-force histories during startup at three high altitudes.

were not applied until around 1.4 s, when the MCC temperature starts to ramp up, as shown in Fig. 1.

V. Results and Discussion

The computations were performed on a cluster machine using 16 processors. Global time steps were varied throughout the computations: 2.5–10 μs were typically used during the initial transient when the change of flow physics was mild, and 1–2.5 μs were used when strong flow physics such as combustion, shock transitions, and shock stem jumping over the TEG exit were occurring. These time steps correspond to Courant–Friedrichs–Lewy numbers ranging approximately from 0.1 to unity. It was known to the design engineers that nozzle side load will be large for sea-level testing. Hence, only the side loads at altitudes of 61,000, 75,000, and 100,000 ft with the nozzle extension attached are of primary interest, as well as those for the stub nozzle at sea level. The hypothetical case for full nozzle extension firing at sea level was added for demonstration and for comparison purposes. Table 1 shows the run matrix. The results of the startup transients at the four altitudes (including the hypothetical sea-level case) are presented first, followed by the results of the startup and shutdown transients for the stub nozzle.

A. Startup Transients at Altitudes

For upper-stage engines, nozzle side loads at high altitudes are of special interest. Figure 8 shows the computed J-2X side-load histories for the startup transients at altitudes of 61,000, 75,000, and 100,000 ft, respectively. In the beginning of the startup process, the transient nozzle flow physics are similar to those of the SSME at sea level [9]. For example, at 61,000 ft, following the description of the physics occurring at different time periods in Fig. 8, the exhaust plume starts out as a core jet flow. As the chamber pressure increases, the core jet flow strengthens and it eventually evolves into a Mach disk flow at around 0.85 s. The supersonic jet behind the Mach disk begins like a solid jet. As the Mach disk flow develops and the size of the Mach disk grows, the supersonic jet starts to separate at the periphery of the disk, forming a conelike jet with a recirculation zone behind the disk. Next, the end of the cone opens up and we have a hollow free-flowing supersonic jet. The outer boundary layers of the core jet and initial Mach disk flows are separated from the nozzle wall at the throat, due to the nozzle contours.

Table 1 Run matrix

Case	Nozzle extension	Area ratio	Transient operation	Altitude, ft	p_∞, atm
1	Attached	92	Startup	100,000	0.011
2	Attached	92	Startup	75,000	0.034
3	Attached	92	Startup	61,000	0.068
4	Attached	92	Startup	0	1.000
5	Detached	35	Startup	0	1.000
6	Detached	35	Shutdown	0	1.000

As the Mach disk flow develops and the size of the Mach disk grows, it imposes an adverse pressure gradient on the nozzle. As the wall boundary layer is not able to negotiate this adverse pressure gradient due to wall friction, the Mach disk flow stays separated, resulting in an oblique shock foot (shock stem) coming off the wall, intersecting the Mach disk and the detached supersonic jet at the triple point. Because the shock and separated flow pattern of this detached hollow supersonic jet flows freely and away from the wall, it is referenced as a FSS [1]. This developing and advancing FSS Mach disk flow is best described by snapshots of time-varying Mach number contours and separation lines shown in Fig. 9. It can be seen that from 1.2 to 1.3375 s the advancing Mach disk and separation lines are relatively horizontal, because the effect of the TEG flow has not taken place yet, although at 1.3375 s the Mach disk has flown past the TEG flow exit ring and the disk size is large enough that the supersonic jet has started to feel the pumping of the exhausting TEG flow. Note that from 1.2 to 1.3375 s, the separation lines, which are formed by connecting all the separation points (or stagnation points), take the shape of a horizontal circle.

Because the ambient pressure at 61,000 ft is 0.034 atm, the external environment behaves effectively as a vacuum pump, drawing both the engine Mach disk and TEG flows out of the thruster faster than at sea level. On the other hand, The Mach disk flow and TEG flow are also trying to influence each other as they establish themselves in the nozzle. It can be seen from Fig. 9 that from 1.2 to 1.3375 s, the TEG is already flowing and possibly drawing the upstream wall pressure down circumferentially. A slight imbalance in the circumferential wall pressure between the TEG exit and the Mach disk flow separation line, caused by the TEG pumping, could cause the Mach disk flow to become asymmetric. That is exactly what happened at 1.35 s, as shown in Fig. 9, in which the entire separation plane slants to the left and the Mach disk is distorted. The left-hand side of the shock stem interacts with the TEG flow first, followed by the right-hand side, and the shock foot steps into TEG flow moments later, causing more disturbance to the Mach disk flow, as shown in the snapshots for 1.3538 and 1.3625 s. These flow disturbances result in the first peak side load shown in Fig. 8. This phenomenon of shock stem and TEG flow interaction was also

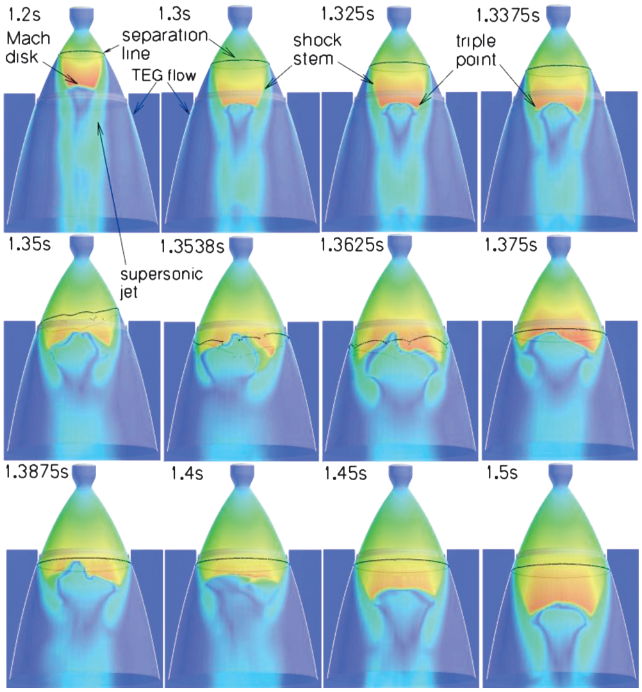

Fig. 9 Mach number contours showing the effect of separation-line jump during startup at 61,000 ft.

referred to as "jump of the separation point" by Watanabe et al. [4] during their work with the hot-firing of LE-7A engine. It is referred to as *jump of the separation line* or *separation-line jump* in this effort to reflect the transient nature and three-dimensionality of the physics. The effect of this jump of the separation line then damps away as the FSS Mach disk wave recovers, as shown in the snapshots of 1.375, 1.3875, and 1.4 s in Fig. 9. The Mach disk flow then resumes its normal advancement, as shown in the final two snapshots at 1.45 and 1.5 s. Note that after 1.3625 s when the separation line has long passed the TEG exit plane, the Mach disk flow is now the stronger party and the TEG flow is wholly entrained into the supersonic jet.

The preceding discussion pertains to the major side-load physics during the startup at 61,000 ft. Using that as a reference point, we examine the effect of altitude on those physics by comparing the side-load histories and corresponding physics of 61,000, 75,000, and 100,000 ft in Fig. 8. It can be seen from Fig. 8 that the major physics happening at 75,000, and 100,000 ft are essentially the same as those of 61,000 ft, except that they occur earlier and the magnitudes are lower. That is because the ambient pressure decreases as the altitude increases. The consequence of lower ambient pressure is the higher pumping effect. That means that the exhaust plume will go out faster, or the various physical events will occur quicker, as altitude increases. This is evidenced by the decreasing times of 0.85, 0.15, and 0.075 s that are required to switch from core flow to FSS Mach disk flow at 61,000, 75,000, and 100,000 ft, respectively. Similarly, the peak side-load occurring times of 1.354, 1.145, and 0.807 s also decrease with the increasing altitude. In addition, the required times for the thruster to flowing full are also shortened as altitude increases, as evidenced by the times of 1.75, 1.65, and 1.525 s for altitudes of 61,000, 75,000, and 100,000 ft, respectively. More important, it can be seen that the result of the shortened side-load event occurring time is the reduction of the residence time for each and every side-load event. For the startup of a film-cooled engine at these altitudes, the dominant side-load physics are the TEG-flow-assisted jump of the separation line, for it generates the peak side load. As the residence time for the jump of the separation line decreases with increasing altitude, the disturbance to the Mach disk flow and wall pressure decreases, and the outcome is the reduced peak side load. This is evidenced by the computed peak side loads of 5.125, 3.149, and 1.101 kN at corresponding altitudes of 61,000, 75,000, and 100,000 ft, respectively. This result is supported by an earlier study in which the peak side load reduced drastically when the ramp time was decreased from 5 to 1 s [9]. It should be mentioned at this time that two distinctive side-load physics, the FSS-to-RSS transition and the RSS breathing at nozzle lip, both observed in the SSME startup at sea level [9], are not observed in these J-2X high-altitude startup cases and will be revisited in the next section. Also note that the J-2X side loads discussed to this point are significantly lower than the SSME sea-level side loads [9].

B. Hypothetical Startup Transient Case at Sea Level

From the result of the preceding high-altitude analyses, it is helpful to examine a hypothetical sea-level full-length nozzle startup case. Figure 10 shows the side-load history from the computational result of this hypothetical case and that of a LE-7A test [4]. The timing of the LE-7A curve was shifted such that the major side-load events for both are compared at about the same time. It can be seen that two distinctive side-load physics are computed to produce significant side loads: a secondary side load caused by the FSS-to-RSS transition at around 1.8 s, and a peak side load generated when the upstream lambda shock foot of the RSS steps into the film coolant flow, or the separation-line jump, at around 2.01 s. The characteristics of the J-2X side-load history exhibited by the two side-load physics look quite different. Leading into the FSS-to-RSS transition, there is a gradual build up of the side force, until reaching its maximum at 1.8 s, then the side force damps gradually to the noise level. On the other hand, the characteristics of the peak side load caused by the jump of the separation line appear to be a sudden jump, followed by a series of decreasing peaks. The characteristics of the two side-load physics of J-2X shown in Fig. 10 are qualitatively similar to those of LE-7A, except the shapes of the LE-7A peaks are broader in time. Fluid–structure interaction could be responsible for the broader peaks of the LE-7A curve. Surprisingly, the quantitative comparisons of the peak side loads of the two film-cooled engines are very close, especially at the separation-line jump. Note that after the FSS-to-RSS transition, RSS flow pattern was maintained throughout the rest of the transient.

The origin of the FSS-to-RSS transition is attributed to the Coanda effect [9]. That is, as described by Coanda [29], the velocities of the turbulently moving particles in the boundary layer of the hollow, free-flowing, cylindrical sheet of a supersonic jet are greater than the jet speed, thus creating underpressure, drawing the jet to the nearby wall to become a RSS flow pattern. In this case, the FSS-to-RSS transition is also potentially boosted by the pumping of the film coolant flow downstream. Continuance of the RSS flow pattern, however, is most likely caused by the enhanced Coanda effect due to the regeneratively cooled nozzle wall, as described in [9]. That is, with a regeneratively cooled nozzle wall, density is higher in the wall boundary layer, leading to higher turbulent viscosity, higher momentum, thinner boundary layer, and lower pressure. The lower pressure at the cooled nozzle wall enhances the Coanda effect and

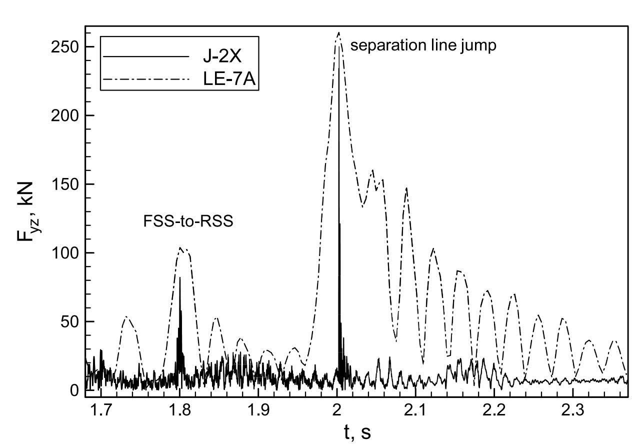

Fig. 10 A comparison of the sea-level startup side-force history of the computed hypothetical case with that of a LE-7A test.

continuously draws the supersonic jet to the wall, which is in contrast to the effect of an adiabatic wall, which repels the supersonic jet from the wall [9].

The FSS-to-RSS transition, however, is not observed in the higher-altitude cases presented earlier. As discussed earlier, the low ambient pressure at higher altitudes has the effect of pumping the flows out axially, as evidenced by the shorter nozzle-flowing-full times as the ambient pressure decreases. The stronger axial pumping effect overtakes the weaker radial Coanda effect, resulting in residence times that are probably too short for the FSS-to-RSS transition to occur [9]. In addition, the aforementioned pumping effect of the TEG flow may not be strong enough to attract the supersonic jet to the wall.

Some might argue that for a TIC nozzle such as J-2X, FSS-to-RSS transition should not happen. That, of course, was challenged by Kwan and Stark's [30] subscale TIC nozzle tests, in which FSS-to-RSS transition was observed. They explained that the TIC nozzle theory was based on steady-state design methods using method of characteristics and are not applicable for transient nozzle flows. Tomita et al. [31] also challenged the TIC theory by performing combustion tests on three subscale nozzles: TIC, compressed truncated ideal, and truncated optimized (TO). Their test results showed that FSS-to-RSS transition occurred in each nozzle when certain ranges of fuel–oxidizer ratio were present. Tomita et al. [31] reasoned that whether RSS takes place or not depends on combustion as well as the nozzle contours. On the other hand, Wang [9] demonstrated that the enhanced Coanda effect helped FSS-to-RSS transition and was the phenomena responsible for maintaining the RSS flow pattern in a regeneratively cooled SSME (TO) nozzle at sea level. He also demonstrated that a short residence time could drastically reduce side loads caused by FSS-to-RSS transition and shock breathing at the lip [9]. The results of the these researches, including those in this effort that show FSS-to-RSS transition occurring at sea level but not at high altitudes with a TIC nozzle, indicate that transient core and film coolant flow properties, combustion, regeneratively cooled nozzle walls, ambient pressures, and residence times are playing more important roles in the RSS formation than nozzle contour.

Furthermore, in a regeneratively cooled TO nozzle such as SSME, the side load caused by the shock breathing at the lip is over twice that of the FSS-to-RSS transition [9], whereas in a film-cooled nozzle with nozzle extension such as the LE-7A [4] and J-2X engines, with compressed truncated ideal and truncated ideal contours, respectively, the side load caused by the separation line jumping is again more than twice that of the FSS-to-RSS transition. These comparisons make the selection of a nozzle contour such as TIC for the sole purpose of avoiding a FSS-to-RSS transition in a full-scale engine a moot point, because the magnitude of the following peak side-load physics such as shock breathing and separation line jumping is more than twice higher than that of a weaker FSS-to-RSS transition.

The breathing of the Mach disk flow in-and-out of the nozzle lip, responsible for the peak side load in the SSME [9], does not appear in the high altitude, as well as the hypothetical sea-level J-2X computations. That is because at sea level, the nozzle extension is too long and the chamber pressure is not high enough to push the Mach disk out of the nozzle extension lip, and hence the nozzle extension is never flowing full. At high altitudes, however, the Mach disk flows are sucked out of the nozzle too quickly, and the transient core and film coolant flow properties are such that the shock waves do not have enough residence time to linger around the lip.

C. Startup and Shutdown Transients of Stub Nozzle at Sea Level

The peak side load computed for the preceding case is significant because the asymmetric force acted on a large surface area, mainly from the nozzle extension. That is why special attention is needed if a hot-firing test is to be performed on a nozzle component at sea-level ambient condition. For this purpose, a stub nozzle would be a good choice theoretically, because the surface area is drastically reduced by removing the nozzle extension. It is therefore helpful to compute the peak side load and to understand the accompanying physics for a stub nozzle operating at sea level, for both startup and shutdown processes.

Figure 11 shows the computed side-load history for the stub nozzle during the startup transient at sea level. It can be seen that the core jet turns into a FSS Mach disk flow at around 1.3 s. Because this is at sea level and the regeneratively cooled nozzle wall enhances the Coanda effect, the FSS-to-RSS transition could occur. However, the shortness of the stub nozzle is such that the shock transition occurs very near to the nozzle lip, making a complete shock transition difficult. In fact, only FSS-to-partial-RSS (PRSS) [9,10] transitions occur at around 1.9 s. This is because with the shock transition occurring so closely to the nozzle lip, portions of the asymmetric petal-like reattachment line [9] of a full RSS are inevitably out of the nozzle, resulting in a PRSS flow pattern. After its establishment, and almost simultaneously, the PRSS breathes several times in and out of the nozzle lip, then leaves the nozzle entirely for all times afterward. Those simultaneous physics create a peak side load of about 26 kN, which is much less than the 80 kN due to FSS-to-RSS transition and 249 kN due to separation line jumping when the nozzle extension is attached. That small peak side load is smaller, because the area in which the asymmetric flow is acting on for the stub nozzle is much less than that with the nozzle extension attached.

Figure 12 shows the computed side-force history for the stub nozzle during the shutdown process. At 5.4 s into the shutdown transient, the Mach disk of the plume retreats to the lip level and then breathes itself across the lip several times as FSS and PRSS, then the retreating Mach disk wave quickly becomes FSS at around 5.5 s. Between 5.5 and 6.1 s, teepeelike OH contours form on the inside of the nozzle and above the lip, as shown in Fig. 13. In addition, a circular separation line is also shown above the Mach disk, which is typical of a FSS flow pattern. The composition of the retreating TEG

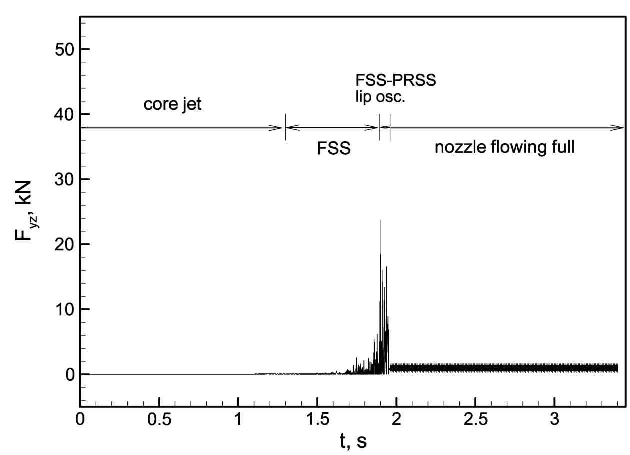

Fig. 11 Computed stub-nozzle side-force history during startup at sea level.

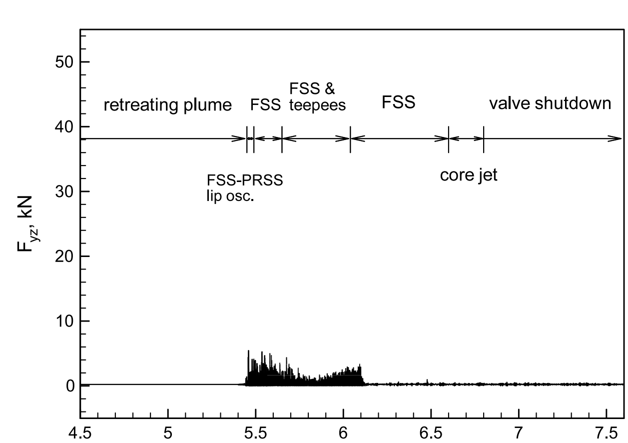

Fig. 12 Computed stub-nozzle side-force history during shutdown at sea level.

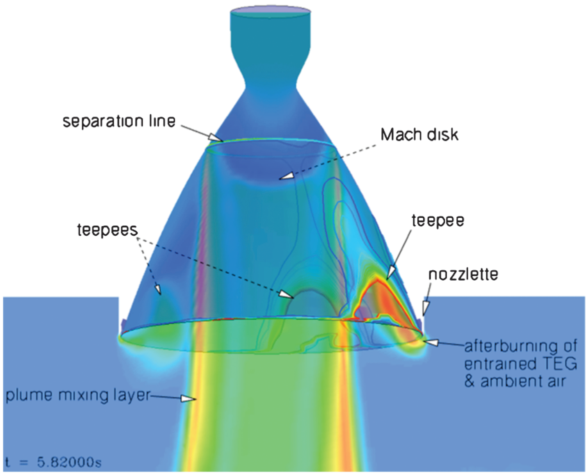

Fig. 13 Temperature contours on a symmetry plane and wall OH concentration contours showing separation line and teepees at 5.82 s into the shutdown process.

flow becomes pure hydrogen at this time. The pure hydrogen then reacts with the entrained air that is sucked into and along the inner nozzle wall to form several triangular-shaped formations, or teepees, on the nozzle wall. These triangular formations start as one and gradually increase to around five, then the numbers decrease and finally disappear at around 6.1 s. Figure 13 shows one teepee in the front half of the nozzle and two teepees in the back half of the nozzle. The timing of the appearance and disappearance of these teepees matches the increase and decrease of hydrogen mass fraction in the TEG flow, as shown in the TEG composition history in Fig. 4. Although the side-load levels are insignificant between 5.5 and 6.1 s, it can be seen from Fig. 12 that this is the only time period that has noticeable side loads, starting with the shock transition and breathing and ending with the disappearance of the teepees. The low side-load level during the shutdown is also attributed to the short nozzle, low aspect ratio, and fast down-ramp rate in particular. Note that the high hydrogen mass fraction and high temperature in the core flow around 7 s, as shown in Figs. 3 and 4, contribute insignificantly to the nozzle side load because the valve essentially shuts down after 6.8 s.

Also note that the physics of the teepees captured here are completely different from those captured during the startup of the SSME [9]. In the SSME startup cases, the teepees are the conical shocks or the petallike reattachment lines of the RSS formation that is being breathed in and out of the nozzle lip.

Table 2 shows a summary of the comparison of the computed J-2X peak side loads of the sea-level startup cases with those of the LE-7A engine tests [4,10]. It can be seen that with the nozzle extension attached, the computed peak side loads for the hypothetical J-2X case at shock transition and at separation line jumping agree reasonably well with those of a LE-7A engine test, also shown in Fig. 10. It appears that for these two full-scale engines, the peak side loads are very close when compared at the same side-load physics. As another example, the side load for SSME during shock transition is 90 kN [9], again quite close to the 80 kN for J-2X and 102 kN for LE-7A, even though SSME is solely a regeneratively cooled engine. It is reasoned that this is because for J-2X and LE-7A engines, the shock transition happens before the occurrence of the separation line jumping, and it happens in the regeneratively cooled part of the nozzle. It is also obvious that a jump of the separation line is the dominant side-load physics for film-cooled engines such as J-2X and LE-7A, firing at sea level with nozzle extension, because its associated side load is 2.5 to 3 times higher than that of FSS-to-RSS transition. Watanabe et al. [4] reported breakage of some of the regenerative cooling tubes during the early hot-firing tests of LE-7A engine when the nozzle extension was attached. Note that for an upper-stage engine such as J-2X, the sea-level case is a hypothetical case and its peak side loads at high altitudes are much smaller, as shown in Fig. 8.

More important, Table 2 shows that the peak side-load reduced drastically without the nozzle extension, for both J-2X and LE-7A engines. For J-2X stub-nozzle startup, or without the nozzle extension, the side-load physics of jump of the separation line are essentially taken away, and the resulting weaker side-load physics of FSS-to-PRSS transition and the simultaneous shock breathing drop the peak side load to 26 from 249 kN, whereas for J-2X stub-nozzle shutdown, the peak side load is negligible (Fig. 12). In summary, the computational result of the J-2X side-load reduction with the stub nozzle agrees with the findings of the LE-7A engine tests [4]; therefore, the stub nozzle is safer for sea-level testing.

Finally, note that the combustion wave physics, present in the early stages of the SSME startup process at sea level due to the accumulation of excess hydrogen and mitigated with the addition of the sparklers [9], did not appear in either J-2X sea-level cases in this study. This is mainly attributed to the faster J-2X startup transient, in which the effective ramp time is about 1.5 s, whereas that for SSME is about 2.5 s. A faster ramp time means less residence time for the combustion wave to occur, as demonstrated in [9]. A secondary reason for the disappearance of the combustion wave is the injection of helium purge gas in the startup transient, which diluted the hydrogen concentration and reduced the reaction rate.

Table 2 Comparison of the startup side loads at sea level

	Side loads, kN		
	J-2X	LE-7A	Physics
	With extension		
First peak	80	102	Shock transition
Second peak	249	259	Separation line jumping
	Without extension		
First peak	26	45	Shock transition and breathing
Second peak	——	——	——

VI. Conclusions

Three-dimensional numerical investigations on the transient nozzle side load have been performed for a preliminary version of the J-2X engine. It is shown that the peak side loads computed for startup operation of the J-2X with attached nozzle extension at high altitudes are caused by the jump of the separation line and decrease in magnitude with increasing altitude. The computed peak side load for startup of a hypothetical test case of the J-2X with attached nozzle extension at sea level is large and also caused by the jump of the separation line. The characteristics of the computed side-load curve and the magnitudes of the side load associated with the shock transition and separation line jumping compare reasonably well with those of a LE-7A test. For the J-2X with a stub nozzle operating at sea level, the computed peak side load of the startup transient is reduced drastically because of the short nozzle, low-asymmetric-flow acting area, and fast ramp-up time; the computed peak side load of the shutdown transient is even smaller for the same reasons and has a faster ramp-down time. These drastic reductions in side load with stub nozzle agree with the findings in the LE-7A test results. Teepeelike formations are captured during the shutdown transient and are caused by the reaction between the retreating TEG flow and the entrained air.

Acknowledgments

This study was partially supported by a NASA Marshall Space Flight Center (MSFC) J-2X nozzle side-load task. The lead author wishes to thank Paul Gradl, Warren Peters, Joe Ruf, and Mike Shadoan for their support of the task and Joe Ruf for reading the manuscript. He also wishes to thank Wallace Welder of Pratt-Whitney Rocketdyne for providing the initial, and Van Luong for providing the final, combustion chamber and nozzle wall temperatures as boundary conditions. Special thanks are given to James Beck of Pratt-Whitney Rocketdyne, Yen-Sen Chen of National Space Organization, and Yasuhide Watanabe of Japan Aerospace Exploration Agency for their insightful suggestions and discussions.

The coauthor wishes to thank Duc Nguyen and Danny Woo of Pratt-Whitney Rocketdyne for providing the engine design and transient sequencing information necessary to create the MSFC J-2X engine system model.

References

[1] Nave, L. H., and Coffey, G. A., "Sea Level Side Loads in High-Area-Ratio Rocket Engines," AIAA Paper 73-1284, Nov. 1973.

[2] Cikanek, H. A., "Characteristics of Space Shuttle Main Engine Failures," AIAA Paper 87-1939, June 1987.

[3] Hagemann, G., Terhardt, M., Frey, M., Reijasse, P., Onofri, M., Nasuti, F., and Ostlund, J., "Flow Separation and Side-Loads in Rocket Nozzles," *4th International Symposium on Liquid Space Propulsion*, DLR, German Aerospace Center, Lampoldshausen, Germany, March 2000, pp. 1–19.

[4] Watanabe, Y., Sakazume, N., and Tsuboi, M., "LE-7A Engine Nozzle Problems During the Transient Operations," AIAA Paper 2002-3841, July 2002.

[5] Shi, J., "Rocket Engine Nozzle Side Load Transient Analysis Methodology—A Practical Approach," AIAA Paper 2005-1860, April 2005.

[6] Winterfeldt, L., Laumert, B., Tano, R., Geneau, J. F., Blasi, R., and Hagemann, G., "Redesign of the Vulcain 2 Nozzle Extension," AIAA Paper 2005-4536, Tucson, AZ, 2005.

[7] Larson, E. W., Ratekin, G. H., and O'Connon, G. M., "Structural Response to the SSME Fuel Feedline to Unsteady Shock Oscillations," *Shock and Vibration Bulletin*, Bulletin 52, Part 2, May 1982, pp. 177–182.

[8] Brown, A. M., Ruf, J., Reed, D., D'Agostino, M. D., and Keanini, R., "Characterization of Side Load Phenomena Using Measurement of Fluid/Structure Interaction," AIAA Paper 2002-3999, July 2002.

[9] Wang, T.-S., "Transient Three-Dimensional Startup Side Load Analysis of a Regeneratively Cooled Nozzle," *Shock Waves*, Vol. 19, No. 3, 2009, pp. 251–264.
doi:10.1007/s00193-009-0201-2.

[10] Yonezawa, K., Yokota, K., Tsujimoto, K., Sakazume, N., and Watanabe, Y., "Three-Dimensional Unsteady Flow Simulation of Compressed Truncated Perfect Nozzles," AIAA Paper 2002-3991, July 2002.

[11] Boccaletto, L., and Lequette, L., "CFD Computation for Rocket Engine Start-Up Simulation," AIAA Paper 2005-4438, July 2005.

[12] Deck, S., and Guillen, P., "Numerical Simulation of Side Loads in an Ideal Truncated Nozzle," *Journal of Propulsion and Power*, Vol. 18, No. 2, 2002, pp. 261–269.
doi:10.2514/2.5965

[13] Shimizu, T., Miyajima, H., and Kodera, M., "Numerical Study of Restricted Shock Separation on a Compressed Truncated Perfect Nozzle," *AIAA Journal*, Vol. 44, No. 3, 2006, pp. 576–584.
doi:10.2514/1.14288

[14] Boccaletto, L., Reijasse, P., and Dussauge, J. P., "Dynamic Behaviour of a Separation Oblique Shock During Film Cooling Transient Injection," AIAA Paper 2007-4003, June 2007.

[15] Boccaletto, L., Reijasse, P., and Dussauge, J. P., "Influence of Film Cooling Injection on Transient Side Loads," AIAA Paper 2007-5474, July 2007.

[16] Reijasse, P., and Boccaletto, L., "Influence of Film Cooling on Nozzle Side Loads," AIAA Paper 2008-392, Jan. 2008.

[17] Tomita, T., Takahashi, M., Sasaki, M., Takahashi, M., Tamura, H., Watanabe, Y., and Tsuboi, M., "Parametric Study on the Influence of a Discontinuous Step in a Nozzle Contour on Side-Load," AIAA Paper 2003-4764, July 2003.

[18] Wang, T.-S., "Multidimensional Unstructured-Grid Liquid Rocket Engine Nozzle Performance and Heat Transfer Analysis," *Journal of Propulsion and Power*, Vol. 22, No. 1, Jan.–Feb. 2006, pp. 78–84.
doi:10.2514/1.14699

[19] Shang, H. M., and Chen, Y.-S., "Unstructured Adaptive Grid Method for Reacting Flow Computation," AIAA Paper 1997-3183, July 1997.

[20] Wang, T.-S., Chen, Y.-S., Liu, J., Myrabo, L. N., and Mead, F. B., Jr., "Advanced Performance Modeling of Experimental Laser Lightcraft," *Journal of Propulsion and Power*, Vol. 18, No. 6, 2002, pp. 1129–1138.
doi:10.2514/2.6054

[21] Chang, G., Ito, Y., Ross, D., Chen. Y.-S., Zhang, S., and Wang, T.-S., "Numerical Simulations of Single Flow Element in a Nuclear Thermal Thrust Chamber" AIAA Paper 2007-4143, June 2007.

[22] Chen, Y.-S., and Kim, S. W., "Computation of Turbulent Flows Using an Extended k-ε Turbulence Closure Model," NASA CR-179204, Oct. 1987.

[23] Wang, T.-S., Droege, A., D'Agostino, M., Lee, Y.-C., and Williams, R., "Asymmetric Base-Bleed Effect on X-33 Aerospike Plume Induced Base-Heating Environment," *Journal of Propulsion and Power*, Vol. 20, No. 3, 2004, pp. 385–393.
doi:10.2514/1.10385

[24] Chen, Y.-S., Cheng, G. C., and Farmer, R. C., "Reacting and Non-Reacting Flow Simulation for Film Cooling in 2-D Supersonic Flows," AIAA Paper 92-3602, July 1992.

[25] Wang, T.-S., Canabal, F., Chen, Y.-S., and Cheng, G. C., "Multiphysics Computational Analysis of a Solid-Core Nuclear Thermal Engine Thrust Chamber," AIAA Paper 2007-7144, June 2007.

[26] Svehla, R. A., and McBride, B. J., "FORTRAN IV Computer Program for Calculation of Thermodynamic and Transport Properties of Complex Chemical Systems," NASA TN D-7056, Jan. 1973.

[27] Steinbrenner, J. P., Chawner, J. R., and Fouts, C., "Multiple Block Grid Generation in the Interactive Environment," AIAA Paper 90-1602, June 1990.

[28] Huynh, H. T., "Analysis and Improvement of Upwind and Centered Schemes on Quadrilateral and Triangular Meshes," AIAA Paper 2003-3541, June 2003.

[29] Coanda, H., "Device for Deflecting a Stream of Elastic Fluid Projected into an Elastic Fluid," U.S. Patent 2,052,869, Sept. 1936.

[30] Kwan, W., and Stark, R., "Flow Separation Phenomena in Subscale Rocket Nozzles," AIAA Paper 2002-4229, July 2002.

[31] Tomita, T., Sakamoto, H., Onodera, T., Sasaki, M., Takahashi, M., Tamura, H., and Watanabe, Y., "Experimental Evaluation of Side Load Characteristics on TP, CTP, and TO Nozzles," AIAA Paper 2004-3678, 2004.

F. Liu
Associate Editor